Visible-IR responsive $BiVO_4/TiO_2$ photoanode with multi-effect point defects for photothermal enhancement of photoelectrochemical water splitting

1 Experimental detail

1.1 Preparation of $BiVO_4/TiO_2$ nanotube arrays photoanode:

(1) TiO_2 nanotube arrays (TNA) were synthesized by two-step anodic oxidation method in a conventional two-electrode system with Ti foil as anode and Pt foil as cathode as reported in the literature.[1]

(2) 20 mL of 0.25 M $Bi(NO_3)•5H_2O$ glycol solution was drop-wisely added into the same volume of 0.25 M KI glycol solution. The mixture was vigorously stirred at room temperature for 30 min, then transferred to a 100 mL Teflon-lined autoclave. The as-prepared TNA substrate was placed at an angle against the wall of the Teflon liner. The autoclave was maintained at 150 ºC for 6 h and then cooled to room temperature. The as-synthesized BiOI/TNA sample was washed extensively with deionized water and ethanol respectively and dried at 80 ºC in oven.

Then, 0.1 mL of 0.1 M $VO(acac)_2$ in DMSO solution was dripped onto the BiOI/TNA electrode to fully cover its surface, which subsequently was calcined at 500 ºC for 3 h with an increasing rate of 2 ºC/min to obtain $BiVO_4$(BVO)/TNA. Then, 1.0 M KOH was used to remove the surface V_2O_5. The obtained sample was washed extensively with deionized water and ethanol respectively and dried at 80 ºC in oven. The pristine BVO/TNA sample was obtained.

1.2 Preparation of Ni-BVO/TNA photoanode:

The detailed synthetic process of Ni-BVO/TNA was the same as that of BVO/TNA sample except the same volume and concentration of mixed glycol solution containing $Ni(NO_3)_2·6H_2O$ and $Bi(NO_3)·5H_2O$ (the mole ratio of Ni/Bi~0.05) was used instead of $Bi(NO_3)•5H_2O$ glycol solution. The obtained sample was labelled as Ni-BVO/TNA.

1.3 Preparation of N-BVO/N-TNA photoanode:

The as-prepared BVO/TNA sample was annealed in NH_3 atmosphere at 500 ºC for 4 h with an increasing rate of 2 ºC/min and then cooled down slowly to room temperature to obtain N-BVO/N-TNA sample.

1.4 Preparation of N,Ni-BVO/N-TNA photoanode:

The as-prepared Ni-BVO/TNA sample was annealed in NH_3 atmosphere at 500 ºC for 4 h with an increasing rate of 2 ºC/min and then cooled down slowly to room temperature to obtain N,Ni-BVO/N-TNA sample.

2 Characterization

X-ray diffraction (XRD) patterns were obtained for crystal phase analysis via using D8 Advance (Bruker, Germany) X-ray diffractometer with Cu Kα radiation (λ=1.5418 Å). The morphology was observed by field-emission scanning electron microscopy (FESEM, JEOL-6700F, Japan) at 20 kV and Energy-dispersive X-ray spectroscopy (EDS, Oxford Energy 350 X-ray energy spectrum analyzer) was employed for the elemental analyses. High-resolution transmission electron microscopy (HR-TEM, Tecnai G220, FEI, USA) images were applied to analyze the microstructures and crystal facets. X-ray photoelectron spectra (XPS) were performed on an ESCALAB 250Xi photoelectron spectrometer (ThermoFisher Scientific, USA) with Al Kα (1486.6 eV) as the X-ray source set at 150 W and a pass energy of 30 eV for high-resolution scan. UV-vis-IR diffuse reflection spectra (DRS) were recorded on a UV-vis-IR spectrophotometer (Varian, Cary 5000, American). Photoluminescence (PL) spectra were taken at room temperature with a fluorescence spectrometer (Hitachi U-4100, Japan) with an excitation at 420-nm light. Raman spectra were recorded on a Renishaw Raman system model 1000 spectrometer at an excitation wavelength of 532.15 nm. Electron paramagnetic resonance (EPR) spectra were measured at room temperature with an EPR spectrometer (Bruker 500, Germany).

3 PEC measurements

All PEC measurements were carried out in the Na_2SO_4 (0.5 M) with a potassium phosphate buffer (0.5 M, pH=7). PEC performances were measured using a CHI660D electrochemical workstation in a standard three-electrode system with the as-prepared samples, Pt sheet and Ag/AgCl electrode as working counter and reference electrodes, respectively. The vis-IR light source was generated by a 300 W Xe lamp equipped with

UVCUT400 (λ>400 nm) filter while visible light was obtained by equipping with UV-IR filter (400 nm<λ<780 nm) on the same Xe lamp. In this work, the incident light intensity remained about 60 mW/cm^2 by adjusting the distance between the light source and the quartz window of the reactor no matter when we used visible light or vis-IR light irradiation. Prior to the measurement, the edges of working electrodes were sealed with epoxy resin to ensure the irradiated area of 1 cm^2 and the electrolyte was purged with N_2 flow for 30 minutes to remove the dissolved O_2. Transient photocurrent density (TPD) was measured under a chopped light irritation (light on-off cycles: 50 s) at a bias potential of +1.23 V *vs.* reversible hydrogen electrode (RHE). The linear-sweep voltammogram (LSV) was measured with a scan rate of 5 mV/s under different conditions. The electrochemical impedance spectroscopy (EIS) was determined at the open circuit potential under an alternating current perturbation signal of 10 mV over a frequency range of 1 MHz-10 mHz under illumination. Mott-Schottky (M-S) plots were obtained by measuring the capacitance at dark with a potential step of 10 mV at a frequency of 1000 Hz. LSV, EIS, and M-S tests were performed after the testing temperatures were constant under irradiation.

The electrochemically active surface areas (ECSAs) were qualitatively compared by measuring the double-layer capacitance under a potential window from 0.2 to 0.3 V *vs.* RHE. Last, all the results were converted to RHE according to the formula [S1]:[2]

$$E_{RHE} = E_{Ag/AgCl} + 0.0591pH + 0.1976 \quad \text{(S1)}$$

4 Calculations

The bandgap of each photoanode was calculated based on the formula [S2]:

$$\alpha h\nu = A\,(h\nu - E_g)^n \quad \text{(S2)}$$

where α is the absorption coefficient, h is the Planck constant, ν is the incident light frequency, A is the absorbance, E_g is the bandgap and the value of n is 2 or 1/2. For BVO/TNA as an *n*-type indirect bandgap semiconductor, n is 1/2.[3]

To calculate the applied bias photon-current efficiency (ABPE) the following equation (S3) was used:[4]

$$ABPE = \frac{J \times (1.23 - V_{app})}{P_{in}} \times 100\% \quad \text{(S3)}$$

Where J represents photocurrent density (mA/cm^2), V_{app} is the applied potential (*vs.*

RHE), and P_{in} is the incident light intensity (60 mW/cm^2).

To quantify the contributions of the suppressing surface charge separation, Na_2SO_3 (0.5 M) was used as the hole scavenger for measuring the surface charge transfer efficiencies (η_{trans}) using the following equations (S4):[5]

$$\eta_{trans} = \frac{J_{H_2O}}{J_{Na_2SO_3}} \times 100\% \quad \text{(S4)}$$

where J_{H_2O} and $J_{Na_2SO_3}$ are the photocurrent densities collected in the 0.5 M potassium borate electrolyte without and with Na_2SO_3 in the Na_2SO_4 (0.5 M)+potassium phosphate buffer (0.5 M, pH=7), respectively.

The Faradaic efficiency (η_{FE}) and oxygen evolution were calculated by the gas chromatography system in an air-tight reactor at 1.23 V *vs.* RHE. The co-doped BVO/TNA photoanode was used as the anode with Pt plate electrode as cathode and Ag/AgCl electrode as the reference electrode. The electrolyte was 0.5 M Na_2SO_4 with a potassium phosphate buffer (0.5 M, pH=7). The vis-IR light resource (60 mW/cm^2) was the same with that used in the previous PEC measurements.

The solar-to-hydrogen (STH) conversion efficiency of co-doped BVO/TNA photoanode was calculated using the following equation:[2]

$$STH = \frac{1.23 \times J \times \eta_{FE}}{P_{in}} \times 100\% \quad \text{(S5)}$$

where J is the operating photocurrent density and η_{FE} is the Faradaic efficiency which was obtained at 1.23 V *vs.* RHE.

5 Results and discussions

5.1 FESEM

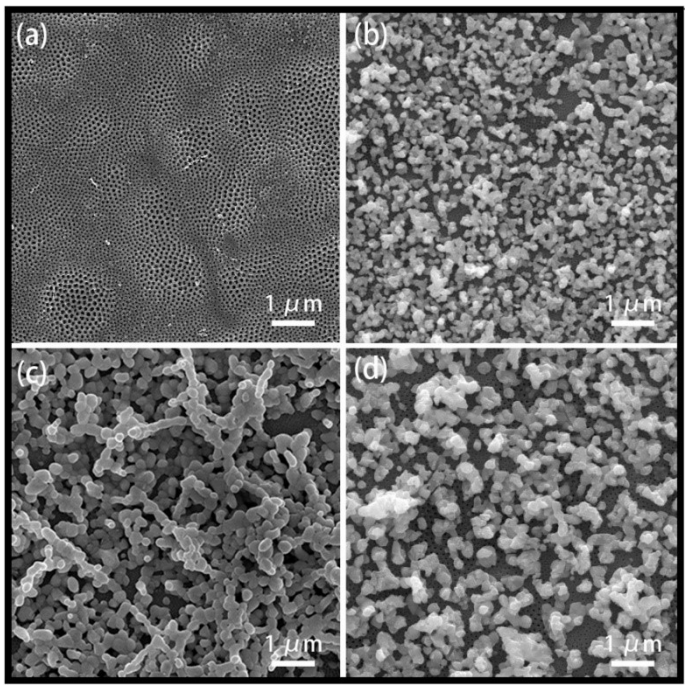

Fig. S1 FESEM images of (a) TNA, (b) BVO/TNA, (c) Ni-BVO/TNA, and (d) N-BVO/N-TNA samples.

5.2 HR-TEM

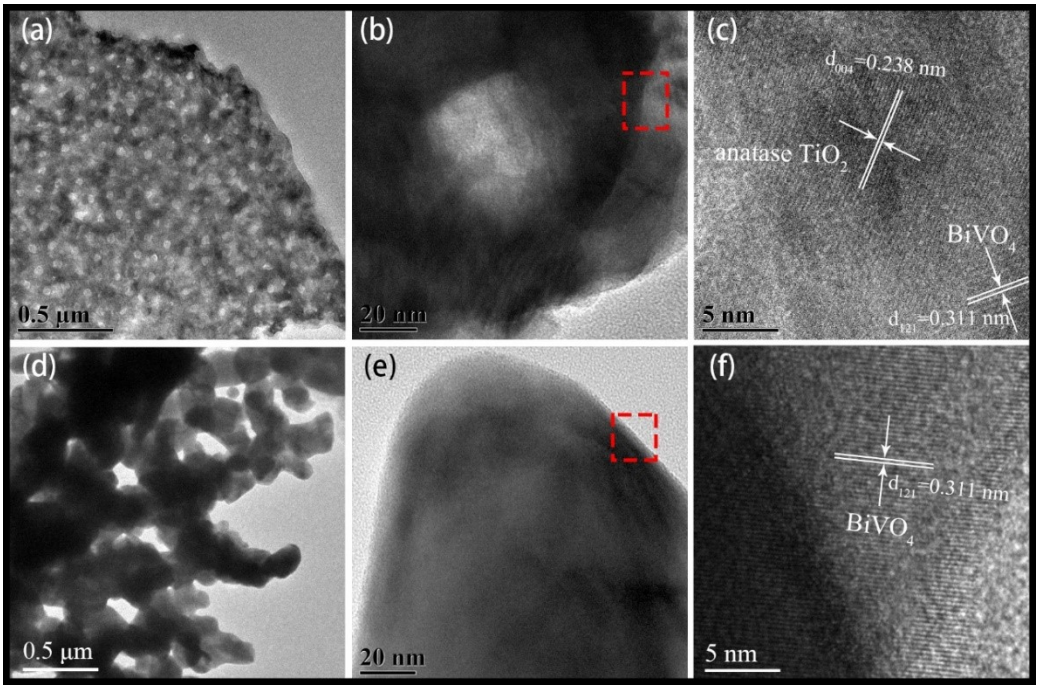

Fig. S2 TEM images for (a, b) doped TNA and (d, e) doped BVO microscopic structure of N,Ni-BVO/N-TNA photoanode. (c, f) HR-TEM images obtained from **Fig. S2b** and **S2e**, respectively.

5.3 XPS spectra

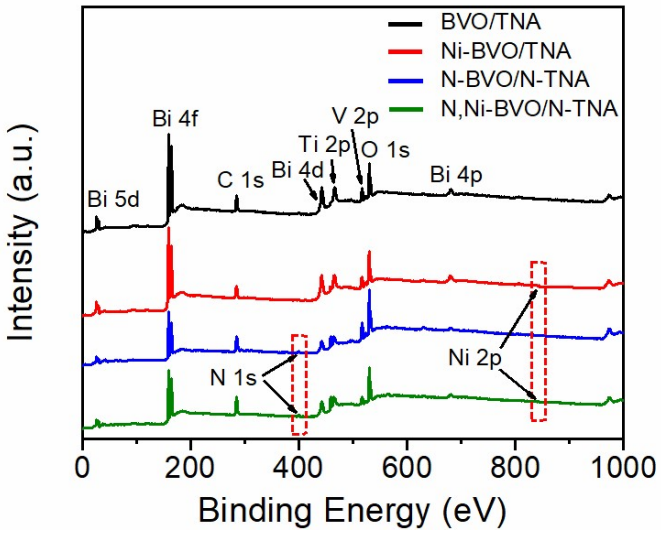

Fig. S3 XPS survey spectra of undoped and doped BVO/TNA photoanodes.

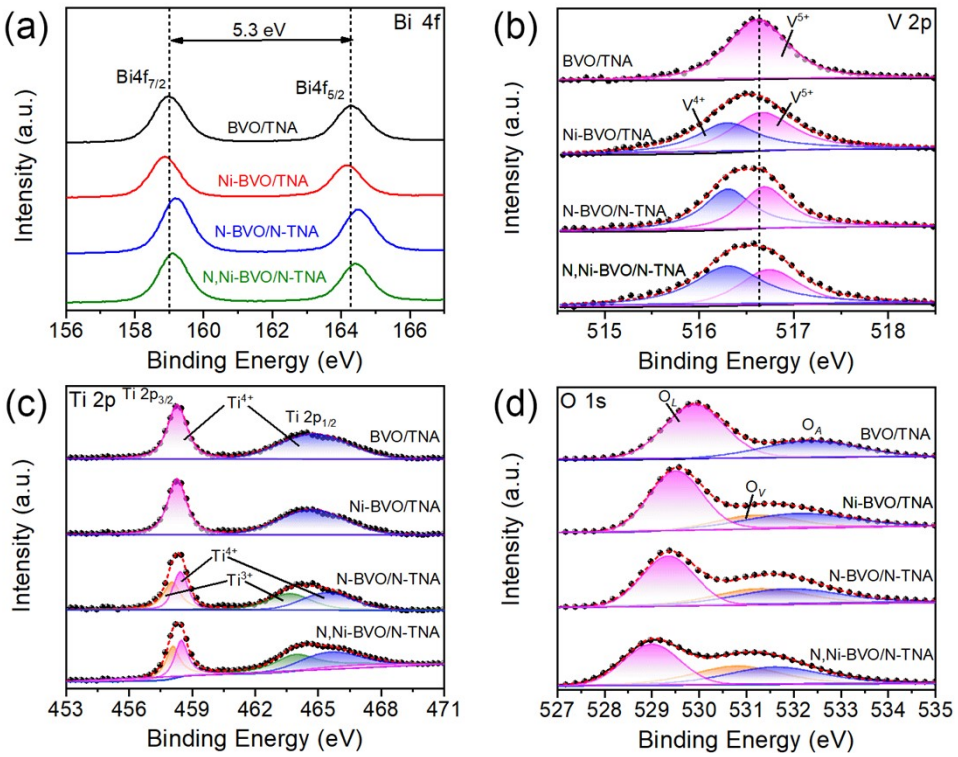

Fig. S4 High resolution XPS Bi 4f (a), V 2p (b), Ti 2p (c) and O 1s (d) spectra of N,Ni-BVO/N-TNA photoanode.

In Fig. S4a, the binding energies located at 159.0 eV (Bi $4f_{7/2}$) and 164.3 eV (Bi $4f_{5/2}$) of BVO/TNA are corresponded to Bi^{3+} species. The spin orbit splitting difference of 5.3 eV is coincident with the literatures [6, 7] But for Ni-doped sample, the Bi 4f peaks all shifted to lower binding energies, because of the electronegativities of Ni (1.8) stronger than that of the substituted V (1.6) via the newly-formed O-Bi-O-Ni-O bond, resulting in the decreasing electron cloud density around Bi atoms. Conversely， the introduction of N element into BVO/TNA caused the increased binding energy of Bi 4f compared with pure sample, owing to the weaker electronegativity of N (3.0) compared to that of O (3.5) in the new O-Bi-N-V-O connection. When co-doping was implemented, the peak shift of Bi 4f fell in the middle. Moreover, doped photoanodes showed the asymmetric V $2p_{3/2}$ signals, which were decomposed into two sub-peaks at 516.3 and 516.7 eV, corresponding to the surface V^{4+} and V^{5+} species, respectively,[8] while pristine BVO/TNA only had one peak for V^{5+} species (Fig. S4b). In addition, the content ratio of V^{4+}/V^{5+} over co-doped sample estimated by the area ratio of characteristic peaks was higher than that of any other BVO/TNA sample from the data listed in Table S1.

Although the formation mechanism was different, Ni or N doping both can result in the presence of V^{4+} highly relevant to O_V.[6, 8] The above-mentioned results indicate that co-doping modification boosts the formation of most V^{4+} ions in the BVO lattice, also meaning that most O_V existed in the surface BVO.

The high-resolution XPS Ti 2p spectra of pure BVO/TNA (Fig. S4c) is characterized by a doublet occurring at 458.3 eV (Ti $2p_{3/2}$) and 464.5 eV (Ti $2p_{1/2}$) corresponding to Ti^{4+} while Ni doping has hardly no effect on the Ti 2p,[9] demonstrating that the absence of Ni element in the TNA substrate. The Ti 2p core level XPS spectrum divides into two sub-peaks and the one at the binding energy of 458.0 eV attributing to Ti^{3+},[9] which originates from the substitution of N^{3-} for O^{2-} and is observed on both N-doped and co-doped photoanodes.[10]

Fig. S4b depicts that the O 1s spectrum over pristine BVO/TNA is decomposed into two peaks located at 529.8 eV and 532.4 eV which can be assigned to the lattice oxygen (O_L) and adsorbed oxygen (O_A).[10] A new O 1s split peak at 531.2 eV over each doped photoanode corresponding to O_V [6] is observed and gradually enhances with the increased kinds of dopants, whose content percentages are listed in Table S2. Further, compared to undoped one, the peak locations of these three oxygen-containing species over doped photoanodes shift slightly to lower binding energy, which is due to co-doping effect.[6, 11] The high-resolution XPS results demonstrate the concentration of oxygen vacancies and the concomitant V^{4+} and Ti^{3+} species increased after co-doping.

5.4 Raman spectra

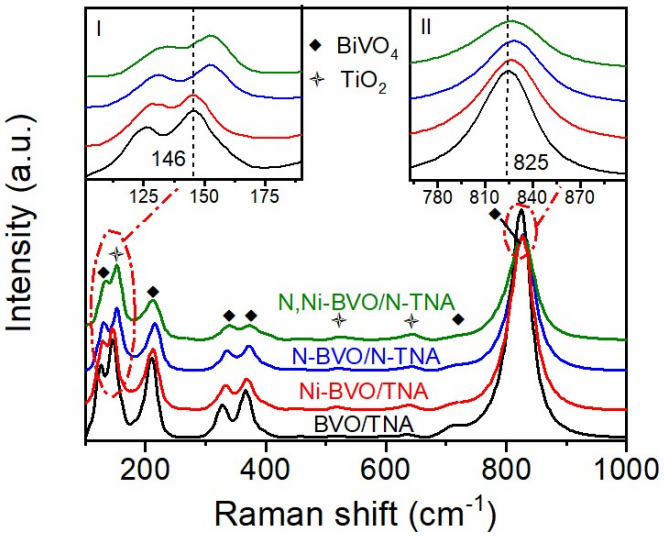

Fig. S5 Raman spectra of undoped and doped BVO/TNA photoanodes.

Raman spectra of all BVO/TNA photoanodes further confirm the crystalline structure and deficient state (Fig. S5). As seen, the vibrational peaks located at 126.0, 210.5, 327.9, 366.7, 713.4 and 824.0 cm^{-1} could be attributed to monoclinic BVO, which are in good agreement with literatures.[12, 13] The scattering peaks in the Raman spectra at 144.9, 518.3, and 638.0 cm^{-1} come from anatase TiO_2.[14] It is observable that N or Ni doping can cause lower crystallinity and more surface defects from XRD and XPS results, which leads to weaker Raman characteristic peaks of doped samples than that of undoped one. As shown in the inset I and II, the first main peak at 144.9 cm^{-1} belonged to TNA is blue-shifts induced by O_V only for N-containing samples,[9] thus indirectly manifesting Ni dopant-induced O_V is absent from TNA. In contrast, the strong peak appeared at 824.0 cm^{-1} assigned to symmetric V-O vibrations in VO_4^{3-} units is affect at both N and Ni dopant to produce a growing blue-shift.[6, 12]

5.5 Thermal effect of photoanodes under visible light

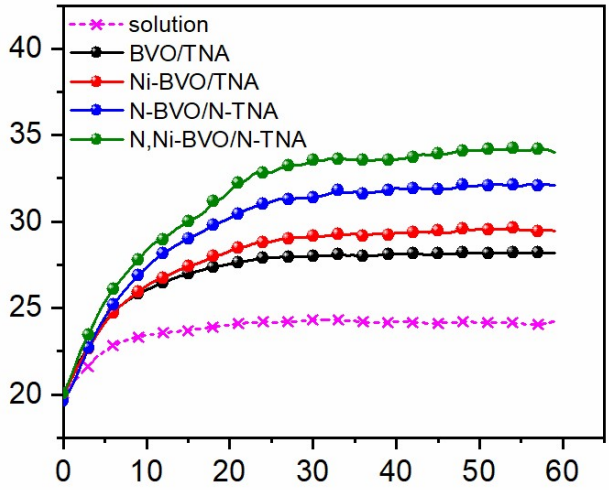

Fig. S6 Thermal effect of all photoanodes in 0.5 M potassium phosphate buffer (pH=7) solution under visible light.

5.6 PEC stability

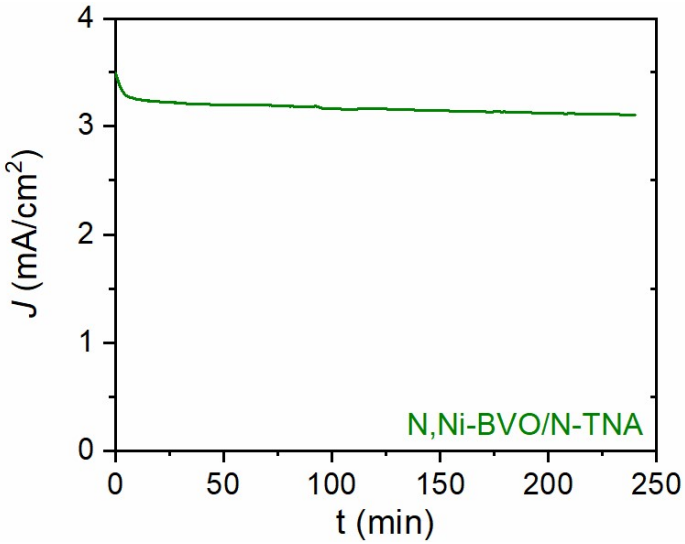

Fig. S7 Long-time TPD over co-doped photoanode under vis-IR light illumination.

5.7 LSV and ABPE without Na_2SO_3

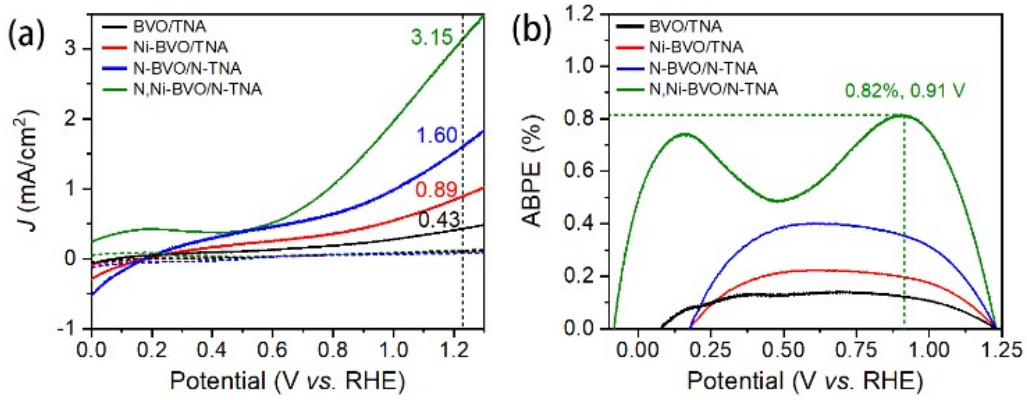

Fig. S8 LSV curves of all photoanodes (a) without Na_2SO_3 under dark and vis-IR light. (b) the relative ABPEs calculated from (a). The solid lines: photocurrent; the dash lines: dark current.

5.8 Faradaic efficiency

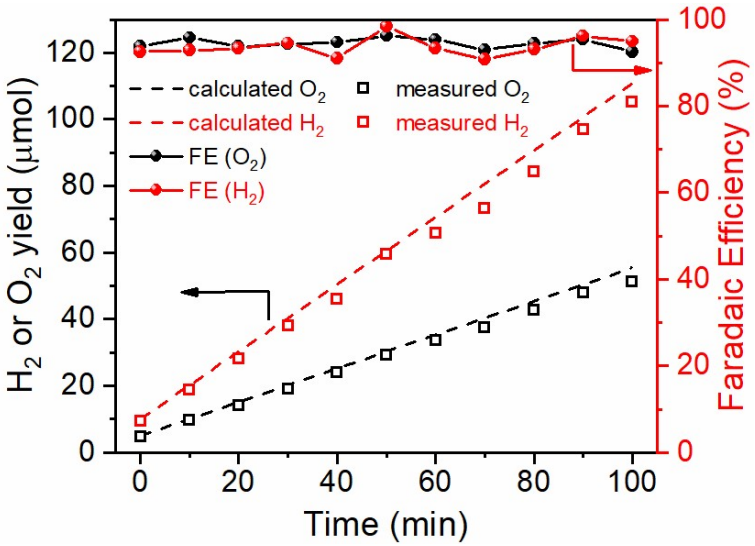

Fig. S9 Faradaic efficiency of N,Ni-BVO/N-TNA photoanode for hydrogen and oxygen evolution.

5.9 PL spectra

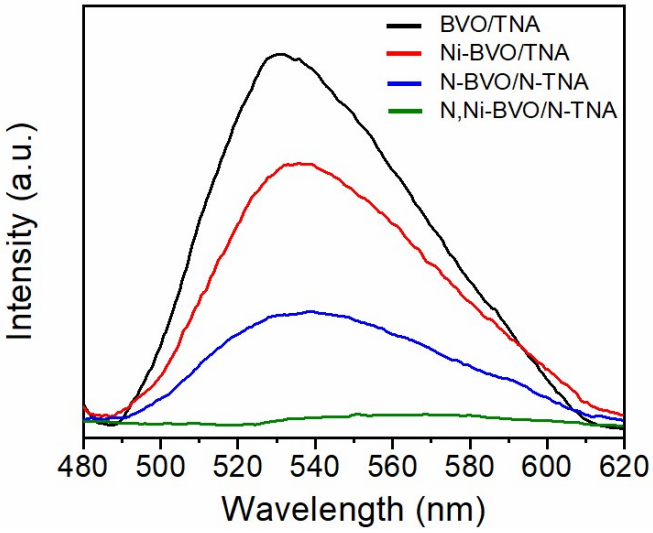

Fig. S10 PL spectra of undoped and doped BVO/TNA photoanodes under vis-IR light.

5.10 EIS plots

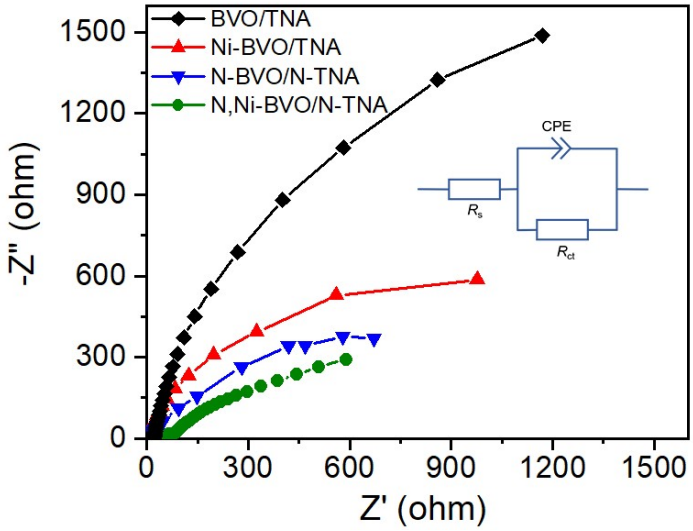

Fig. S11 EIS plots of all BVO/TNA photoanodes at the open circuit potential under vis-IR light illumination at the constant solution temperatures.

5.11 LSV and η_{trans}

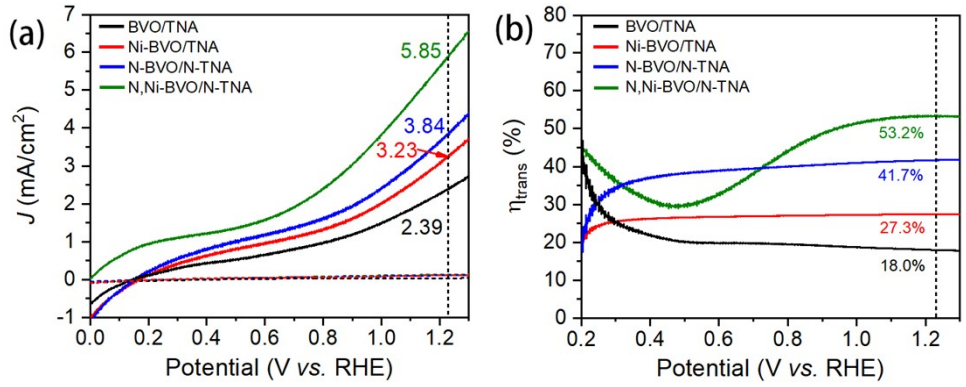

Fig. S12 LSV curves of all photoanodes (a) with Na_2SO_3 under dark and vis-IR light. (b) Charge transfer efficiencies (η_{trans}) at the photoanode/electrolyte interface of undoped and doped samples when the solution temperatures are stable. The solid lines: photocurrent; the dash lines: dark current in Fig. S11a.

5.12 Electrochemical active surface area (ECSA)

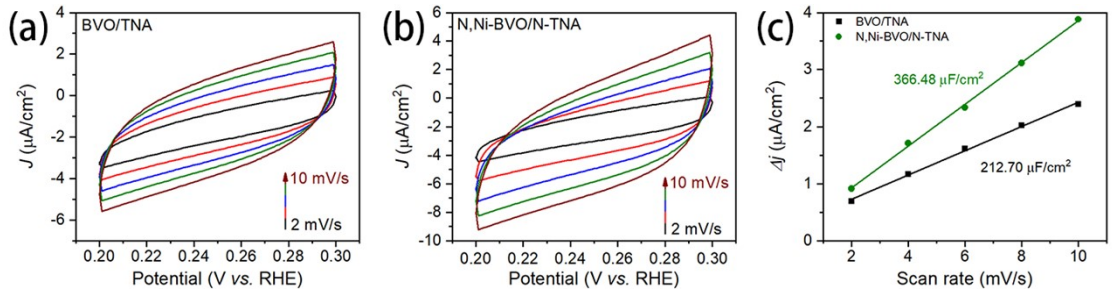

Fig. S13 CVs of (a) undoped and (b) co-doped photoanodes measured in a non-Faradaic region (0.20-0.30 V *vs.* RHE) at different scan rates. (c) Charging current density differences of anodic and cathodic currents ($\Delta J = J_a - J_c$) *vs.* the scan rate of different photoanodes.

ECSAs were calculated from the electrochemical double layer capacitance (C_{dl}) using cyclic voltammetry (CV) results (Fig. S12a and b). The difference in current density (ΔJ) of the anodic (J_a) and the cathodic (J_c) sweeps ($\Delta J = J_a - J_c$) *vs.* scan rate was plotted in Fig. S12c. The linear slope of the plot is equivalent to twice the C_{dl}, and

thus the slope value can be used to estimate the relative changes in the ECSAs. It is noted that co-doped sample exhibits a larger slope value than undoped photoelectrode, indicating of more abundant PEC active sites.

5.13 M-S plots and XPS-valence band (VB) spectra

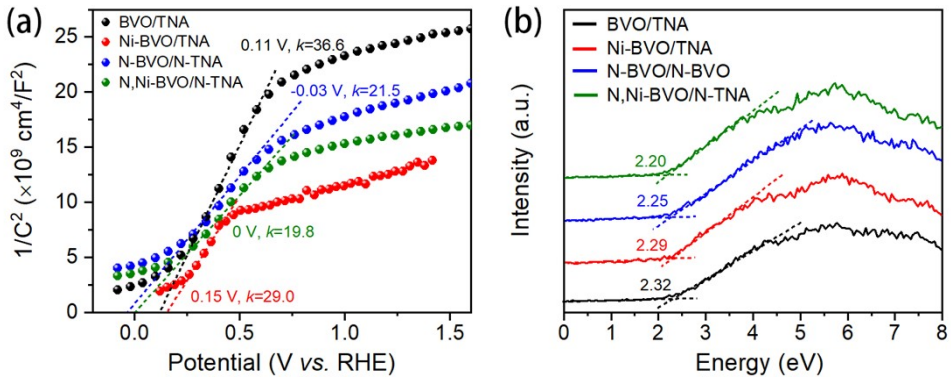

Fig. S14 (a) M-S plots measured at the steady solution temperatures and (b) XPS-VB spectra of all BVO/TNA photoanodes.

Firstly, from M-S plots (Fig. S13a) the flatband potential (E_{fb}) for each BVO/TNA sample was obtained. The intercept equals to E_{fb} +k_BT/e (V_{RHE}), where E_{fb} is the flatband potential, k_b is the Boltzmann constant with the value of 1.380×10^{-23} J/K, T is the absolute temperature (298 K), e is the electronic charge with a value of 1.602×10^{-19} C.[15] Therefore, the E_{fb} of BVO/TNA, Ni-BVO/TNA, N-BVO/N-TNA, and N,Ni-BVO/N-TNA is 0.084, 0.124, 0, and 0.03 V, respectively. Secondly, from XPS-VB spectra (Fig. S13b), the bandgap between flatband potential to the valence band maximum (VBM) for BVO/TNA, Ni-BVO/TNA, N-BVO/N-TNA, and N,Ni-BVO/N-TNA is estimated as 2.32, 2.29, 2.25, and 2.20 eV, respectively. Therefore, the VBM position of BVO/TNA, Ni-BVO/TNA, N-BVO/N-TNA, and N,Ni-BVO/N-TNA is 2.40, 2.41, 2.25, and 2.23 V, respectively. Last, combining with the bandgap energy obtained from the Tauc plots (Fig. 2b), the dominant photon energy of the intrinsic transition from VBM to CBM is 2.47, 2.44, 2.36, and 2.29 eV, respectively. Hence the CBM position is determined at -0.07, -0.03, -0.11, and -0.07 V for BVO/TNA, Ni-BVO/TNA, N-BVO/N-TNA, and N,Ni-BVO/N-TNA, respectively. The detailed energy band alignments of all photoanodes are illustrated in Fig. S14.

5.14 Energy band alignment

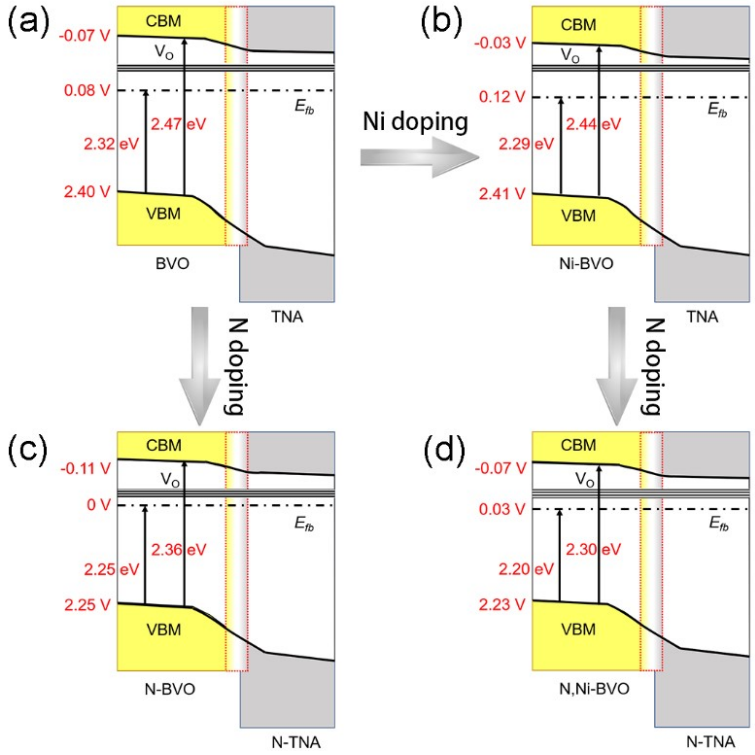

Fig. S15 Energy band alignment of all photoanodes: (a) BVO/TNA, (b) Ni-BVO/TNA, (c) N-BVO/N-TNA, (d) N,Ni-BVO/N-TNA.

Table S1 Peak areas of V^{4+} and V^{5+} species and the area ratio of V^{4+}/V^{5+}.

Samples	Peak area		Area ratio
	V^{5+} (eV)	V^{4+} (eV)	V^{4+}/V^{5+}
BVO/TNA	31050 (516.6)	-	-
Ni-BVO/TNA	17258 (516.7)	14494 (516.2)	0.84
N-BVO/N-TNA	14987 (516.7)	16642 (516.3)	1.11
N,Ni-BVO/N-TNA	12842 (516.7)	20164 (516.3)	1.57

Table S2 The percentage content of O_L, O_A, and O_V calculated from XPS O 1s spectra.

Samples	O_L (eV)	O_A (eV)	O_V (eV)
BVO/TNA	68.8% (529.9)	31.2% (532.4)	-
Ni-BVO/TNA	55.2% (529.5)	26.2% (532.1)	18.5% (531.2)
N-BVO/N-TNA	42.5% (529.3)	30.8% (531.9)	26.7% (531.3)
N,Ni-BVO/N-TNA	37.4% (529.0)	31.5% (531.6)	31.1% (530.9)

Table S3 The photocurrent density and ABPE at 1.23 V *vs.* RHE of co-doped photoanode in this work and previously reported BVO/TNA and N or Ni doped BVO (TNA)-based photoanodes toward PEC water splitting.

Samples	Co-catalyst	Electrolyte	Light source	Photocurrent density mA/cm^2	ABPE	Ref.
BVO/TNR[a]	Co-Pi	0.5 M Na_2SO_4	AM1.5G	2.36	0.52%	16
BVO/TNA	-	0.2 M Na_2SO_4	visible	0.336	-	17
BVO/TNR	AuNPs	0.5 M Na_2SO_4	vis-IR	-1.21	-	18
BVO/Ta:TNG[b]	-	0.1 M K_3PO_4/KH_2PO_4	vis-IR	1.77	0.24%	19
BVO/Au/TNA	-	0.5 M K_2SO_4	AM1.5G	0.123	-	20
BVO/Ta:TNW[c]	-	0.5 M KPi	AM1.5G	2.1	-	21
BVO/TNR	Co-Pi	0.1 M Na_2SO_3	AM1.5G	2.27	0.57%	22
BVO/G/TiO_2	-	0.1 M K_2SO_4	AM1.5G	0.13	0.12%	23
BVO/TiO_2	-	0.1 M K_3PO_3	AM1.5G	0.44 (1.6 V_{RHE})	-	24
BVO/TiO_2	Co-Pi	0.5 M Na_2SO_4	AM1.5G	1.61	-	25
BVO/TNA	-	0.1 M Na_2SO_4	visible	2.73 (1.6 V_{RHE})	-	26
BVO/TNA	-	0.05M Na_2SO_4	visible	0.0058	-	13
BVO/TiO_2	-	0.5M Na_2SO_4	AM1.5G	1.12	0.71%	27
BVO/TiO_2	-	0.1 M K_2HPO_4	visible	1.25	-	28
BVO/TiO_2	-	0.5 M Na_2SO_4	AM1.5G	0.94	-	29
Ni-BVO	-	0.5 M Na_2SO_4	visible	0.91 (1.6 V_{RHE})	-	30
Ni-BVO-O_V	-	0.2 M Na_2SO_4	AM1.5G	2.39	0.55%	6
Ni-BVO	-	0.1 M KPi	vis-IR	1.36	0.49%	7
BVO/TiO_2	-	0.1 M Na_2SO_4	AM1.5G	2.1	-	3
N,Ni-BVO/N-TNA		0.5 M Na_2SO_4	vis-IR	3.15	0.82%	This work

[a] TNR: TiO_2 nanorods
[b] TNG: TiO_2 nano sheets
[c] TNW: TiO_2 nanowires

Table S4 Fitted results of Nyquist plot from the equivalent circuit.

Samples	R_s (Ω cm^2)	R_{ct} (Ω cm^2)
BVO/TNA	17.53	5083.35
Ni-BVO/TNA	7.25	1461.26
N-BVO/N-TNA	6.65	1229.33
Ni,N-BVO/N-TNA	9.82	1050.45

References

1. F. Li, B. Dong and S. Feng, *Int. J. Hydrogen Energ.*, 2019, **44**, 29986-29999.
2. J. W. Yang, I. J. Park, S. A. Lee, M. G. Lee, T. H. Lee, H. Park, C. Kim, J. Park, J. Moon, J. Y. Kim and H. W. Jang, *Appl. Catal. B: Environ.*, 2021, **293**, 120217.
3. H. Chen, J. Li, W. Yang, S. E. Balaghi, C. A. Triana, C. K. Mavrokefalos and G. R. Patzke, *ACS Catal.*, 2021, **11**, 7637-7646.
4. T. W. Kim and K. S. Choi, *Science*, 2014, **343**, 990-994.
5. X. Lu, K.-h. Ye, S. Zhang, J. Zhang, J. Yang, Y. Huang and H. Ji, *Chem. Eng. J.*, 2022, **428**, 131027.
6. D. Kong, J. Qi, D. Liu, X. Zhang, L. Pan and J. Zou, *Trans. Tianjin Uni.*, 2019, **25**, 340-347.
7. S. Saxena, A. Verma, K. Asha, N. K. Biswas, A. Banerjee, V. R. Satsangi, R. Shrivastav and S. Dass, *Int. J. Hydrogen Energ.*, 2020, **45**, 26746-26757.
8. F. Li, L. Zhang, X. Chen, Y. L. Liu, S. G. Xu and S. K. Cao, *Phys. Chem. Chem. Phys.*, 2017, **19**, 21862-21868.
9. Y. Zhao, L. Zhu, Y. Yu, F. Gao, W. Wang, D. Chen and X. Zhao, *Catal. Today*, 2020, **355**, 563-572.
10. M. Wang, C. Niu, Z.-J. Dong, Y.-S. Che, D. Dong, H.-Y. Zheng and C.-X. Yang, *J. Inorg. Mater.*, 2014, **29**, 807-813.
11. M. Wang, Q. Liu, Y. Che, L. Zhang and D. Zhang, *J. Alloy. Compd.*, 2013, **548**, 70-76.
12. C. Regmi, Y. K. Kshetri, T.-H. Kim, D. Dhakal and S. W. Lee, *Mol. Catal.*, 2019, **470**, 8-18.
13. W. Zhou, T. Jiang, Y. Zhao, C. Xu, C. Pei and H. Xue, *J. Alloy. Compd.*, 2019, **777**, 1152-1158.
14. X. Wang, Z.-C. Guan, P. Jin, Y.-Y. Tang, G.-L. Song, G.-K. Liu and R.-G. Du, *Corros. Sci.*, 2019, **157**, 247-255.
15. H. Pang, X. Meng, H. Song, W. Zhou, G. Yang, H. Zhang, Y. Izumi, T. Takei, W. Jewasuwan, N. Fukata and J. Ye, *Appl. Catal. B: Environ.*, 2019, **244**, 1013-1020.
16. Z. Guo, J. Wei, B. Zhang, M. Ruan and Z. Liu, *J. Alloy. Compd.*, 2020, **821**, 153225.
17. D. Hongxing, L. Qiuping and H. Yuehui, *R. Soc. Open. Sci.*, 2018, **5**, 180728.
18. Q. Shi, Z. Li, L. Chen, X. Zhang, W. Han, M. Xie, J. Yang and L. Jing, *Appl. Catal. B: Environ.*, 2019, **244**, 641-649.
19. J. Li, J. Bai, X. Niu, X. Li, S. Chen, J. Wang and B. Zhou, *Int. J. Hydrogen Energ.*, 2018, **43**, 18202-18210.
20. Y. Lu, Y. Chu, W. Zheng, M. Huo, H. Huo, J. Qu, H. Yu and Y. Zhao, *Electrochim. Acta*, 2019, **320**, 134617.
21. J. Resasco, H. Zhang, N. Kornienko, N. Becknell, H. Lee, J. Guo, A. L. Briseno and P. Yang, *ACS Cent. Sci.*, 2016, **2**, 80-88.
22. R. Tong, X. Wang, X. Zhou, Q. Liu, H. Wang, X. Peng, X. Liu, Z. Zhang, H. Wang and P. D. Lund, *Int. J. Hydrogen Energ.*, 2017, **42**, 5496-5504.
23. S. Yousefzadeh, M. Faraji and A. Z. Moshfegh, *J. Electroanal. Chem.*, 2016, **763**, 1-9.
24. S. Ho-Kimura, S. J. A. Moniz, A. D. Handoko and J. Tang, *J. Mater. Chem. A*, 2014, **2**, 3948–3953.
25. B. Y. Cheng, J. S. Yang, H. W. Cho and J. J. Wu, *ACS Appl. Mater. Interfaces*, 2016, **8**, 20032-20039.
26. R. Wang, J. Bai, Y. Li, Q. Zeng, J. Li and B. Zhou, *Nano-micro Lett.*, 2017, **9**, 14.
27. Q. Liu, R. Mo, X. Li, S. Yang, J. Zhong and H. Li, *Appl. Surf. Sci.*, 2019, **464**, 544-551.

28. Q. Zhu, Z. Xu, Q. Yi, M. Nasir, M. Xing, B. Qiu and J. Zhang, *Mater. Chem. Front.*, 2020, **4**, 3234-3239.
29. R. Shi, H. F. Ye, F. Liang, Z. Wang, K. Li, Y. Weng, Z. Lin, W. F. Fu, C. M. Che and Y. Chen, *Adv. Mater.*, 2018, **30**, 1705941.
30. M. Lei, J. Liu, Y. Huang, Y. Dong, S. Zhou, H. Zhao, Z. Wang, M. Wu, Y. Lei and Z. Wang, *Nanotechnology*, 2019, **30**, 445403.